JACS
JOURNAL OF THE AMERICAN CHEMICAL SOCIETY

ARTICLE

pubs.acs.org/JACS

# Aryl C−H Amination by Diruthenium Nitrides in the Solid State and in Solution at Room Temperature: Experimental and Computational Study of the Reaction Mechanism

Amanda Kae Musch Long,[†] George H. Timmer,[†] József S. Pap,[†,‡] Jamie Lynn Snyder,[†] Renyuan Pony Yu,[†] and John F. Berry*[,†]

[†]Department of Chemistry, University of Wisconsin—Madison, 1101 University Avenue, Madison, Wisconsin 53706, United States
[‡]Department of Chemistry, University of Pannonia, 8200 Veszprém, Hungary

Supporting Information

**ABSTRACT:** Diruthenium azido complexes $Ru_2(DPhF)_4N_3$ (**1a**, DPhF = *N*,*N*′-diphenylformamidinate) and $Ru_2(D(3,5\text{-}Cl_2)PhF)_4N_3$ (**1b**, D(3,5-$Cl_2$)PhF = *N*,*N*′-bis(3,5-dichlorophenyl)formamidinate) have been investigated by thermolytic and photolytic experiments to investigate the chemical reactivity of the corresponding diruthenium nitride species. Thermolysis of **1b** at ∼100 °C leads to the expulsion of $N_2$ and isolation of $Ru_2(D(3,5\text{-}Cl_2)PhF)_3NH(C_{13}H_6N_2Cl_4)$ (**3b**), in which a nitrogen atom has been inserted into one of the proximal aryl C−H bonds of a D(3,5-$Cl_2$)PhF ligand. A similar C−H insertion product is obtained upon thawing a frozen $CH_2Cl_2$ solution of the nitride complex $Ru_2(DPhF)_4N$ (**2a**), formed via photolysis at −196 °C of **1a** to yield $Ru_2(DPhF)_3NH(C_{13}H_{10}N_2)$ (**3a**). Evidence is provided here that both reactions proceed via direct intramolecular attack of an electrophilic terminal nitrido nitrogen atom on a proximal aryl ring. Thermodynamic and kinetic data for this reaction are obtained from differential scanning calorimetric measurements and thermal gravimetric analysis of the thermolysis of $Ru_2(D(3,5\text{-}Cl_2)PhF)_4N_3$, and by Arrhenius/Eyring analysis of the conversion of $Ru_2(DPhF)_4N$ to its C−H insertion product, respectively. These data are used to develop a detailed, experimentally validated DFT reaction pathway for $N_2$ extrusion and C−H functionalization from $Ru_2(D(3,5\text{-}Cl_2)PhF)_4N_3$. The diruthenium nitrido complex is an intermediate in the calculated reaction pathway, and the C−H functionalization event shares a close resemblance to a classical electrophilic aromatic substitution mechanism.

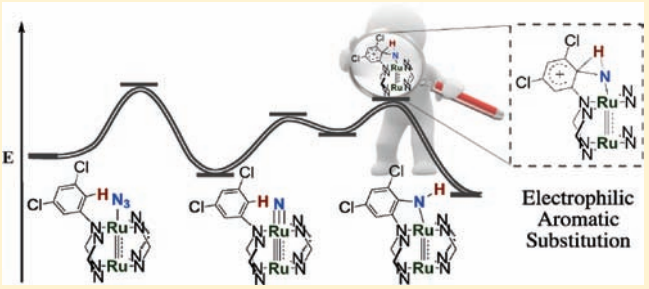


## 1. INTRODUCTION

Direct functionalization of C−H bonds is an emerging methodology at the frontier of synthetic chemistry.[1−5] One of the most successful C−H functionalization methods currently employed is carbenoid/nitrenoid insertion into C−H bonds, reactions that are chiefly mediated by metal−metal bonded $Rh_2$ or $Ru_2$ catalysts,[1−5] though other types of catalysts have also been developed.[1−8] Convincing indirect evidence for an intermediate dirhodium carbene complex such as **A** has been presented,[6] and the corresponding nitrene species such as **B** are also assumed to be the key catalytically relevant intermediates that perform C−H insertion.[2,9,10] No direct evidence for the formation of species **A**, **B**, or any other compound having a metal−metal/metal−ligand multiply bonded core had been provided until our group reported the generation and low-temperature characterization of the diruthenium nitrido species **C**,[11] a close structural analogue of **A** and **B**, as illustrated in Chart 1.

Compound **2a** can be prepared by low-temperature photolysis of the corresponding azido precursor.[11,12] Though the diphenylformamidinate (DPhF) ligands were employed to enhance the stability of the highly oxidized $Ru_2^{7+}$ center, we found that **2a** is nonetheless very reactive and is only stable in frozen solution at liquid nitrogen temperature, conditions that preclude its isolation as a solid. An attempt to generate a diruthenium nitride in the solid state by azide thermolysis using the more electron-withdrawing D(3,5-$Cl_2$)PhF ligand was found instead to lead to a product having a nitrogen atom inserted into one of the aryl C−H bonds of the D(3,5-$Cl_2$)PhF ligand to form the insertion product **3b** (Scheme 1).[13] Because of their electrophilicity,[10,14] late transition metal nitrido compounds have recently been considered as precursors to aziridenes,[15] and recent reports have highlighted the possibility of alkyl C−H functionalization by highly reactive nitrido species.[16−19] Our report is the first to implicate a nitrido species in the amination of aryl ($sp^2$) C−H bonds. The mechanism of this transformation is therefore of considerable interest.

**Received:** May 12, 2011
**Published:** July 11, 2011





dx.doi.org/10.1021/ja203993p | *J. Am. Chem. Soc.* 2011, 133, 13138–13150

**Chart 1. (Top) Carbenoid and Nitrenoid Models (A, B) and the Terminal Nitride Structural Analogue (C); (Middle) Ligand Key for Compounds a (DPhF = *N,N′*-Diphenylformamidinate) and b (D(3,5-$Cl_2$)PhF = *N,N′*-Bis-(3,5-dichlorophenyl)formamidinate); (Bottom) Compounds of Note for the Two Ligand Systems (a, b) Presented in This Work**

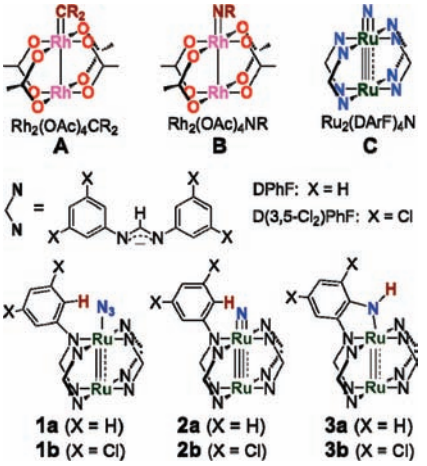


**Scheme 1. (a) Direct Solid-State Thermolytic Generation of 3 from 1; (b) Photolytic Conversion of 1a To Form 2a in Frozen $CH_2Cl_2$ (*i*), Followed by N-Atom Insertion into the Aryl C−H Bond To Form 3a (*ii*)**

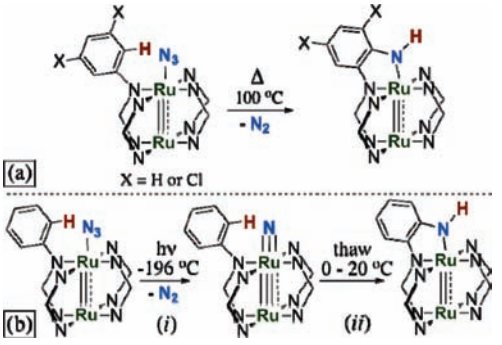


Though it has been proposed that the reaction in Scheme 1(a) proceeds through a nitrido intermediate, and similar proposals have been made for alkyl C−H insertions by putative nitrides of Co,[16a] Fe,[16b] Ni,[17] U,[18] Rh,[19] and Ir,[19,20] direct evidence for such a mechanism is currently lacking. In this article, we provide such evidence. Herein we show that when a frozen dichloromethane solution of the photochemically generated $Ru_2(DPhF)_4N$ (**2a**) is thawed, insertion of the nitrido N atom into one of the aryl C−H bonds occurs readily at room temperature and below, yielding $Ru_2(DPhF)_3NH(C_{13}H_{10}N_2)$ (Scheme 1(b)), analogous to the result of the thermolytic reaction. Reported here are studies of these reactions, and a detailed computational analysis of the reaction mechanism of **1b** to **3b** using DFT methods, which is found to follow the general reaction course shown in Scheme 2, where the conversion of **2b** to **3b** via transition states **TS2** and **TS3** is consistent with an electrophilic aromatic substitution mechanism.

**Scheme 2. General Reaction Coordinate and Key Structures Following the Reaction Course from 1b to 3b**

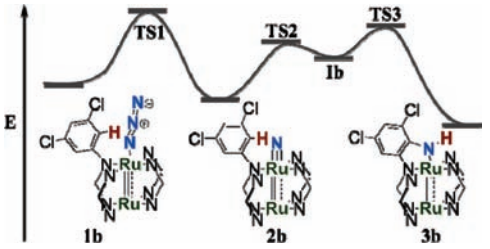


## 2. EXPERIMENTAL SECTION

**2.1. Materials.** Unless otherwise noted, all syntheses were carried out under a dry $N_2$ atmosphere using established Schlenck techniques, while product isolation was achieved under ambient conditions. Solvents were dried and purified according to standard techniques. The ligands HDPhF, HD($D_5$)PhF, and HD(3,5-$Cl_2$)PhF, as well as the corresponding ruthenium precursors, $Ru_2(OAc)_4Cl$, $Ru_2(DPhF)_4Cl$, $Ru_2(D(3,5\text{-}Cl_2)PhF)_4Cl$, $Ru_2(DPhF)_4N_3$, and $Ru_2(D(3,5\text{-}Cl_2)PhF)_4N_3$, were prepared according to published procedures.[12]

**2.2. General Thermolytic Preparation.** Three methods were used for bulk thermolysis of compounds **1a** and **1b**: a KBr pressed-pellet method, thermolysis *in vacuo*, and thermolysis via thermal gravimetric analysis (TGA). Thermolysis of **1a** ground in a KBr pellet was designed for facile infrared (IR) spectroscopic monitoring. The KBr pellet was heated *in vacuo* at the bottom of an Erlenmeyer flask immersed in an oil bath, and it was only exposed to air when it was periodically removed from this flask to take an IR spectrum.

*2.2.1. Thermolytic Preparation of $Ru_2(DPhF)_3NH(C_{13}H_{10}N_2)$ (**3a**).* Thermolysis *in vacuo* of dark violet solid **1a** (28.7 mg, 0.0280 mmol) at 160 °C for 48 h yielded a dark violet solid mixture containing **3a** in addition to side products. The solid mixture was extracted with dry $CH_2Cl_2$ (10 mL) and crystallized from $CH_2Cl_2$ and hexanes to yield small X-ray-quality violet crystals of **3a** after 7 days at −20 °C. Yield: 20.7 mg, 74.2%. Anal. Calcd for **3a**·$H_2O$: C, 61.4; H, 4.53; N, 12.4. Found: C, 61.4; H, 4.40; N, 12.4 (CHN analyzed using $V_2O_5$ catalyst). Solid samples of **3a** exposed to air were found to be highly hygroscopic, as indicated by the presence of water in the elemental analysis. MALDI-TOF: $m/z$ = 1001.2 [**3a**]$^+$. UV−vis: $\lambda$ ($\varepsilon$) = 525 nm (8900). IR (KBr, cm$^{-1}$): 3405 b, 3055 m, 3021 w, 1940 w, 1644 m, 1617 s, 1582 s, 1538 m, 1261 w, 1008 w, 808 m, 571 w.

*2.2.2. Thermolytic Preparation of $Ru_2[(D(3,5\text{-}Cl_2)PhF)_3NH\text{-}(C_{13}H_6Cl_4N_2)]$ (**3b**).* Thermolysis *in vacuo* of purple solid **1b** (15.6 mg, 0.0152 mmol) at 100 °C for 24 h directly yielded the purple solid **3b**. Yield: 15.1 mg, 98.9%. X-ray-quality crystals were grown over 3 days upon dissolution of **3b** in minimal (3 mL) $CH_2Cl_2$ and layering the resulting solution with dry hexanes at room temperature. Anal. Calcd for **3b**: C, 40.34; H, 1.83; N, 8.15. Found: C, 40.34; H, 2.09; N, 8.16. MALDI-TOF: $m/z$ = 1548.2 [**3b**]$^+$. UV−vis: $\lambda$ ($\varepsilon$) = 271 nm (39 000), 497 nm (6600). IR (KBr, cm$^{-1}$): 1581 m, 1564 m, 1539 s, 1503 w, 1427 m, 1330 m, 1252 w, 1215 m, 1159 w, 1111 m, 936 m, 856 w, 805 m, 729 w, 669 m.

**2.3. Photolytic Preparation of 3a.** Conversion of the azide precursor **1a** to the intermediate nitrido species **2a** was achieved according to our previously published procedure by irradiation of frozen $CH_2Cl_2$ solutions at 350 nm in quartz electron paramagnetic resonance (EPR) tubes immersed in a quartz dewar of liquid nitrogen.[11]

This technique was optimized utilizing quartz EPR tubes (4 mm outer diameter) to contain 1 mL aliquots of the dichloromethane solution of **1a** immersed in liquid nitrogen within a quartz dewar

inside the photolytic reactor. With sufficiently dilute solutions of **1a** (0.050−0.200 mM), maximum conversion of **1a** to **2a** was observed, with a yield of 85% nitride based on quantitative EPR measurements of the product mixture. Incomplete photolytic conversion of the azide to the nitride under these conditions has proven nontrivial based upon the opacity of frozen dichloromethane and the relative penetration depth of the UV radiation. The unphotolyzed azide remaining in solution did not, however, interfere with the yield or kinetics of the insertion reaction as monitored by UV−vis spectroscopy *in situ*, as the fractional azide was a constant presence and became part of the baseline correction.

A frozen solution of the violet azide **1a** in $CH_2Cl_2$ (0.200 mM) was prepared in standard quartz EPR tubes at −196 °C and then held in liquid nitrogen in a quartz dewar and photolyzed for 6 h to form **2a**. The resulting frozen pink solution was carefully thawed, resulting in a clear peach-colored solution of the amido product **3a**. Solvent was removed *in vacuo*, and the residue was analyzed. MALDI-TOF: $m/z$ = 1001.1 $[\mathbf{3a}]^+$. UV−vis: $\lambda$ ($\varepsilon$) = 525 nm (8900). IR (KBr, $cm^{-1}$): 3404 b, 3055 m, 1938 w, 1642 w, 1615 s, 1580 s, 1536 m, 1260 w, 806 w.

**2.4. Physical Measurements.** Photolysis of a frozen solution of **1a** was achieved with light from 350 nm mercury vapor lamps in a Rayonet RPR-200 photochemical reactor. FTIR spectra were measured on a Bruker Tensor 27 spectrophotometer using dry KBr pellet techniques. Low-temperature EPR spectra were acquired on a Varian Line spectrometer equipped with a Varian E102 microwave bridge interfaced with a Linux system. An Oxford Instruments ESR-900 continuous-flow helium flow cryostat and an Oxford Instruments 3120 temperature controller were used to control the sample temperature. A Hewlett-Packard 432A power meter was used for microwave power calibration, with measurement conditions as follows: 9.3832 GHz, 5.000 G modulation amplitude, 2450.0 G center field, 2700.0 G sweep width, 0.6325 mW power, 30.0 dB gain, 2.56 ms time constant, and 3.4 K. Matrix-assisted laser desorption/ionization (MALDI) mass spectrometry data were recorded at the Mass Spectrometry Facility of the Chemistry Department Instrumentation Center of the University of Wisconsin−Madison, using a Bruker Reflex II mass spectrometer in positive ion detection mode with 25 kV acceleration voltage, equipped with a 337 nm laser, a reflectron, a time-of-flight analyzer, and delayed extraction. Differential scanning calorimetry (DSC) measurements were performed on a Thermal Advantage Q-100 differential scanning calorimeter fitted with a TA refrigerated cooling system and TA autosampler. TGA of dinitrogen extrusion and thermal conversion was monitored on a TA Instruments TGA Q-500 build model 203 in conjunction with the TA Instruments Universal Analysis 2000 software package. UV−vis−NIR spectroscopic measurements were performed with a StellarNet miniature fiber-optic dip-probe spectrometer and spectrum analyzer equipped with SpectraWiz software for processing.

**2.5. X-ray Structure Determinations at 100 K.** A dark purple crystal of **3b** with approximate dimensions 0.20 × 0.20 × 0.04 $mm^3$ was selected under oil under ambient conditions, attached to the tip of a MiTeGen MicroMount tool, mounted on a goniometer in a stream of cold nitrogen at 100(1) K, and centered in the X-ray beam using a video monitoring system.

Crystal evaluation and data collection were completed primarily at the University of Wisconsin−Madison on a Bruker-AXS Quazar SMART APEX-II diffractometer with Mo Kα radiation at 100(1) K.

The data were collected using a routine to survey reciprocal space to the extent of a full sphere, to a resolution of 0.70 Å, and were indexed by the SMART program.[21] The data were corrected for Lorentz and polarization effects. Absorption corrections were based on a function fitted to the empirical transmission surface as sampled by multiple equivalent measurements.[21] Systematic absences in the diffraction data were consistent with the monoclinic space group $C2/c$, and the structure was solved using direct methods using both SHELX and OLEX2 software packages.[22−24] Crystals of **3b** were found to exhibit axial ligand disorder common among axially substituted paddlewheel-type compounds.[25]

**2.6. Density Functional Theory Calculations.** The reaction of the azide **1b** to form the nitrido species **2b** by $N_2$ extrusion and the subsequent C−H functionalization yielding the amido product **3b** was investigated using spin-unrestricted DFT methods. These calculations also provide the basis for modeling the observed kinetic isotope effect (KIE) of the conversion of **2a** to **3a** in $CH_2Cl_2$. All calculations were carried out with the Orca 2.8.0 program package.[26] All geometry optimizations, including transition-state searches, were run using the BP86[27,28] functional with all-electron def2 basis sets from the Karlsruhe group,[29] which are automatically recontracted in Orca for use with the scalar relativistic zeroth-order regular approximation (ZORA). The geometry optimization basis set, B1, includes an accurate polarized triple-ζ basis set (def2-TZVP) for the diruthenium core as well as the atoms directly involved in the modeled reactions: N1, N2, and N3 of the azide moiety as well as carbon (C1) and hydrogen (H1) atoms at the site of aryl C−H bond activation. The remaining non-hydrogen atoms used the polarized double-ζ basis set, def2-SVP, and the remaining hydrogen atoms used the unpolarized version (SV). Optimizations included a van der Waals correction from Grimme,[30,31] increased integration grid (Grid4 in Orca convention), and tight SCF convergence criteria. The appropriate def2 auxiliary basis sets[32] were used with the efficient RI approximation.[33] The input geometries for **1b** and **3b** were obtained from crystallographic data, and **2b** was generated by deleting $N_2$ from the azide moiety of **1b**. Complexes **1b**, **2b**, and **3b** were optimized in both doublet and quartet spin states. Two relaxed surface scans (RSSs) that constrained the N1−N2 bond distance were used to convert **1b** to **2b** and produce initial guess structures for **TS1**. The first RSS lengthened the N1−N2 distance from 1.2 to 2.0 Å in 0.1 Å increments, and then from 2.0 to 4.0 Å in 0.25 Å increments on the quartet surface to form $^4$**2b** + $N_2$. The second RSS decreased the N1−N2 distance beginning from the nitride $^2$**2b** and dinitrogen with the same increments as the first, resulting in formation of azide $^2$**1b**. The initial guess structure for **TS2** was generated from RSSs that contracted the N1−C1 distance beginning from $^{4,2}$**2b** (N1−C1, 2.5 to 1.5 Å in 0.1 Å increments) for both spin states. An intermediate, **Ib**, located between **TS2** and **TS3** was found by unconstrained geometry optimization of the **TS2** structures. To locate **TS3**, the distance between N1 and H1 beginning from **Ib** was contracted from 2.0, 1.75, 1.65, and 1.60 to 1.0 Å in 0.1 Å increments.

An H-atom abstraction pathway was investigated by contracting the H1−N1 distance of $^{4,2}$**2b** from 2.0 to 1.0 Å in 0.1 Å increments to form a nitrene complex, leaving a radical on C1. A direct pathway from **1b** to **3b** in which $N_2$ extrusion and C−H functionalization occur in a concerted fashion was also considered; however, it was clear from the RSS modeling of the attack of the azide moiety on the ring that this pathway was highly unfavorable. The RSSs used the ScanTS keyword in Orca that aborts the scan after the highest energy structure is located and begins TS optimizations from the highest point of the scan utilizing a hybrid Hessian that is exact only for the constrained atoms in the RSS. This method was efficient and successful for all of the TS structures in the present work, except for the H-atom abstraction pathway, which would not optimize.[34] However, this pathway is clearly higher in energy compared to **TS2** and **TS3** and is also inconsistent with the KIE data (*vida infra*). The TS searches used the eigenvector-following algorithm first implemented by Baker.[35] Three minimum energy crossing points (mecps) between doublet and quartet states were found: **mecp1** is between **1b** and **TS1**, **mecp2** is between **Ib** and **TS3**, and **mecp3** is between **TS3** and **3b**. All geometries were verified by numerical frequency calculations using central differences to contain zero imaginary frequencies for local minima and one imaginary frequency along the reaction coordinate for transition states. Transition states were further

verified as such by the larger contribution of zero-point energy to their total energy than for potential energy minima. "Surface crossing" frequency calculations were used to verify the mecp structures.

Single-point energy calculations were performed on all optimized structures using the B2 (def2-TZVP, all atoms) basis set with both BP86 and B3LYP[26,36−39] functionals, with the latter using the RIJ-COSX chain-of-spheres approximation[40] to accelerate calculations of hybrid functionals. A very large integration grid was used for these calculations (Grid5 in Orca). B3LYP/B2 broken-symmetry (BS) single-point calculations that specified two unpaired electrons on one center and one antiferromagnetically coupled unpaired electron on another center ($M_S$ = 1/2) were performed on both quartet and doublet structures.[41] The B3LYP energy of the $N_2$ molecule along with the thermochemical contributions from frequency calculations were added to each **2b**, **TS2**, **Ib**, **TS3**, and **3b** to facilitate comparison across the seven-complex series. We will focus on the results from B3LYP, which consistently yields more accurate energies for transition metal complexes,[40,43] particularly for systems with multiple possible ground-spin states;[44] B3LYP has been the functional of choice in numerous mononuclear reactions such as iron oxo hydroxylation and H-atom abstraction reactions.[45−47] As is typical for pure GGA functionals with no Hartree−Fock exchange, the BP86 results destabilize the quartet states relative to the doublet states (Figure S10), consistent with the observation that Hartree−Fock exchange stabilizes states of higher multiplicity proportional to the amount added.[48]

Unrestricted natural orbitals (UNOs) were used to study the electronic structure of the series of complexes and unrestricted corresponding orbital transformation[39] (UCOs) for the BS solutions. All images were generated using the UCSF Chimera program package.[49] The Avogadro program[50] was used to edit XYZ files for conversion of **2b** to **2a** in modeling the KIE. The COSMO solvent model was used to approximate the effect of $CH_2Cl_2$.[51] Theoretical estimation of the KIE on optimized structures using the DPhF ligand and COSMO was performed by replacing all aryl H atoms with deuterium and evaluating the semiclassical Eyring equation using $\Delta H$ ($KIE_E = \exp((\Delta H_{(D)}^{\ddagger} - \Delta H_{(H)}^{\ddagger})/RT)$), and a tunneling correction due to Wigner was added by multiplying $KIE_E$ by the tunneling ratio ($Q_{t,H}/Q_{t,D}$), where $Q_t = 1 + (h\nu/kT)^2/24$, denoted $KIE_W$.[45,52,53]

## 3. RESULTS AND DISCUSSION

**3.1. Synthesis.** We recently reported the successful preparation and isolation of $Ru_2[(D(3,5\text{-}Cl_2)PhF)_3NH(C_{13}H_6N_2Cl_4)]$ (**3b**), formed via thermolysis of the azide precursor $Ru_2(D(3,5\text{-}Cl_2)PhF)_4N_3$ (**1b**).[13] The *meta*-dichlorinated aryl rings were employed to enhance electron-withdrawing ability, enhance electrophilicity of the proposed nitride intermediate, and facilitate product formation via the *ortho*-/*para*-directing effect of the aryl chlorine atoms. It is, however, remarkable that the electron-poor dichlorinated aryl ring was able to be functionalized in an electrophilic manner. Here we report that the unsubstituted DPhF compound **1a** also undergoes thermolytic conversion to yield the corresponding C−H insertion product $Ru_2(DPhF)_3NH(C_{13}H_{10}N_2)$ (**3a**), which has been characterized crystallographically[54] and spectroscopically. Although the nitrido species **2a** is implied as a reaction intermediate, we sought to verify its intermediacy by preparing **2a** photochemically. In contrast to the well-documented inertness of mononuclear ruthenium nitrides,[10,14] **2a** reacts readily upon thawing to form **3a**. Spectroscopic properties of **3a** formed via either thermolysis or photolysis are quite similar, showing that the C−H inserted product is indeed formed in each case.

**3.2. Single-Crystal X-ray Crystallographic Studies.** The structure of **3b**[13] is presented in Figure 1, and additional crystallographic data can be found in Figures S1 and S2. The overall structure of **3b** reported here contains the paddlewheel motif. However, a loss of symmetry with respect to the ∼$C_4$-symmetric axial azide precursor is observed, resulting from the intramolecular nitrogen insertion into the proximal aryl C−H bond.

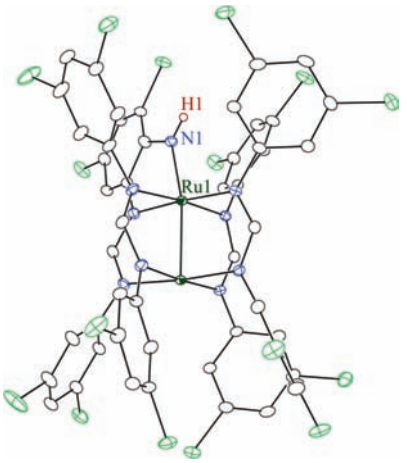


**Figure 1.** Thermal ellipsoid drawing of **3b**[13] with ellipsoids drawn at 30% probability. Non-amido hydrogen atoms are omitted for clarity.

The structure of **3b**[13] has a bound diruthenium core surrounded by four bridging D(3,5-$Cl_2$)PhF or N-functionalized $NH(C_{13}H_6N_2Cl_4)$ ligands. The ruthenium axial positions are disordered, each having a half-occupied amido N atom with a Ru−N bond distance of 2.07 Å, which is inserted into one aryl C−H bond of one of the four bridging ligands. This disorder is demanded by the crystallographic *C*2/*c* symmetry, with a two-fold axis bisecting the Ru−Ru vector. The Ru−Ru distance in **3b** of 2.41 Å is slightly elongated by ∼0.06 Å in comparison to the parent azido compound,[12] which, despite the deviation from linearity along the diruthenium−nitrogen core upon formation of **3b** ($Ru-Ru-N_{(amido)}$ = 164.1° and $C_{(aryl)}-N_{(amido)}-Ru$ = 119.1°), is consistent with the amido ligand being a very strong σ-donor.

**3.3. Thermolytic Methods.** *3.3.1. Vibrational Spectroscopy.* In previous work, resonance Raman spectroscopy with $^{14}N/^{15}N$ isotopic substitution was used to unambiguously identify a feature at 847 $cm^{-1}$ as the Ru≡N stretching frequency of **2a**.[11] This band corresponds to a band of $a_1$ symmetry in the $C_{4v}$ point group and is therefore both IR and Raman active. We therefore were curious whether this band would be visible in a prolonged thermolytic reaction, the conversion of **1a** to **3a**, as its presence would strongly suggest the intermediacy of **2a**. Additionally, the N−H stretch could be monitored in principle, but in practice this band is obscured by water. By gently heating a pressed KBr pellet of **1a** at 60 °C under dynamic vacuum and periodically measuring the IR spectrum of the pellet, the progressive disappearance of the azide peak at 2057 $cm^{-1}$ was found to accompany the temporary emergence of a peak at 849 $cm^{-1}$, which we assign as $\nu$(Ru≡N) of the nitride. The relative intensity of absorbance of this peak is shown in Figure 2. Notably, this peak is not persistent but disappears over the course of the reaction, consistent with the intermediacy of the nitrido compound **2a**. It should be noted that, whereas **2a** is only stable in fluid solution on a time scale of hours (*vide infra*), the data in Figure 2 suggest that this compound is significantly more stable in the solid state. This added stability of **2a** as a solid is likely a result of restricted

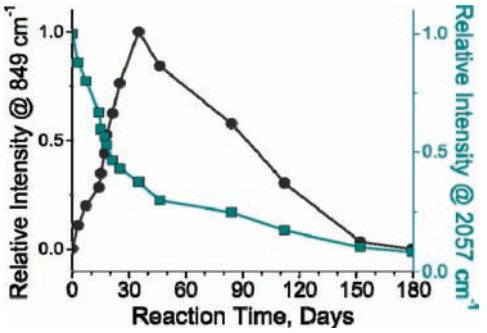


**Figure 2.** Following $\nu$(Ru≡N) at 849 cm$^{-1}$ (black circles) and disappearance of $\nu(N_3)$ at 2057 cm$^{-1}$ (green squares) via IR spectroscopy throughout controlled thermolytic conversion of **1a** to **3a** (KBr pellet form, 60 °C *in vacuo*).

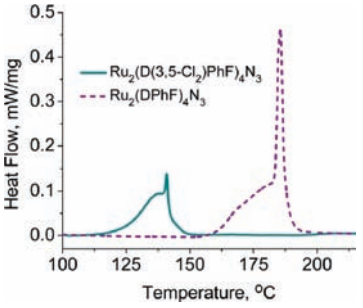


**Figure 3.** DSC plots following thermolytic conversions of **1b** to **3b** (solid blue plot) and **1a** to **3a** (dashed purple plot).

rotation of the phenyl rings in the crystalline state. Lamentably, **2a** is not formed cleanly and could not be isolated separately from **1a** or **3a** using this technique.

*3.3.2. Differential Scanning Calorimetry and Thermal Gravimetric Analysis.* DSC provides a means to observe the thermolytic conversion from **1** to **3** by monitoring the change in heat flow, relative to a blank standard, through the sample in an adiabatic chamber over the course of the reaction. Integration of the DSC signal (in both cases, the peaks were inseparable and were integrated together) provides an experimental $\Delta H$ value for the complete chemical conversion of azide to amido product for both species studied here. For **1b**, $\Delta H = -215.2 \pm 12.2$ kJ mol$^{-1}$, or $-51.42 \pm 2.90$ kcal mol$^{-1}$, is determined from the data shown in Figure 3. The DSC traces for thermolytic conversion of **1b** and **1a** appear to be qualitatively similar. However, TGA results show that in fact **1a** was reproducibly observed to undergo at least one additional transformation, observed to occur upon heating from 120 to 180 °C, and indeed we have observed unidentified byproducts from thermolysis of **1a**. It should therefore be noted that the experimental $\Delta H$ values obtained for conversion of **1a** to **3a** in this manner are unreliable, since this technique yields **3a** and at least one additional side product. The experimental $\Delta H$ value ($-225 \pm 2.5$ kJ mol$^{-1}$, or $-53.8 \pm 0.6$ kcal mol$^{-1}$) for the conversion to **3a** thus includes all chemical transformations and side reactions. However, this method does provide an upper limit for the $\Delta H$ value for the reaction of interest.

TGA was used to monitor the extrusion of $N_2$ from the azido compounds via a direct change in sample mass. As illustrated in Figure 4, the loss of 1.79% mass (28.02 g mol$^{-1}$) over the course

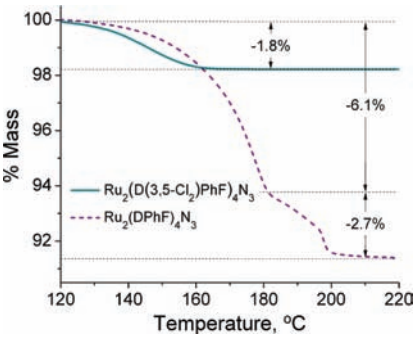


**Figure 4.** TGA plots following the clean thermolytic conversion of **1b** to **3b** (solid blue plot) and the multistep conversion including **1a** to **3a** (dashed purple plot).

of thermolytic conversion of **1b** to **3b** correlates directly with complete liberation of dinitrogen. However, the TGA results for the conversion of **1a** to **3a** indicate the occurrence of more than one simple chemical transformation. The initial sample weight change, corresponding to loss of ~6% of the mass, can only be accounted for by partial decomposition of the organic ligand framework. The extrusion of dinitrogen (2.73% mass) for this conversion does not occur until 180 °C, the last of the signals observed.

Burger and co-workers have also monitored conversion of iridium and rhodium azide precursors to intramolecular "tuck-in" insertion complexes or dimerization products via DSC and TGA measurements.[19] They reported dinitrogen loss observed with onset temperatures beginning at 150 °C for the iridium azide and above 200 °C for the rhodium azide, and experimental $\Delta H$ values of $-27$ and $-36$ kcal mol$^{-1}$, respectively. Energetically, the relatively facile thermolytic conversions reported here for **1a** to **3a** and **1b** to **3b** are supported by the depressed onset temperatures required to initiate dinitrogen loss. Conversions of **1a** and **1b** also release more energy than the Rh and Ir systems do, suggesting that the diruthenium nitrides are inherently higher energy species and are more reactive than the mononuclear Rh or Ir species.

Recrystallization of the product mixture containing **3a** obtained from TGA was performed, and we noted a persistent gray byproduct that we have been unable to identify. Upon crystallization of this gray byproduct from $CH_2Cl_2$ open to air, we obtained crystals of an axial hydroxo complex in low yield, $Ru_2(DPhF)_4OH$.[55] The observation of this product suggests that, in addition to the thermal N−N cleavage to form the diruthenium nitride, homolytic scission of the Ru−N bond may also occur, yielding the $N_3^{\bullet}$ radical, which quickly decomposes to $N_2$ and the reactive $Ru_2$(II,II) species (presumed to be the gray byproduct), which is then oxidized by air as shown in Scheme 3, to yield the hydroxo complex. The hydroxo complex is not formed from **3a**. We note that this hydroxo complex has only been observed under thermolytic conditions when the compound is exposed to air.

**3.4. Photolytic Methods.** Photolytic preparation of the terminal nitrido compound **2a** was achieved with 350 nm radiation over 6 h following our previously reported protocol.[11] As the solutions of **2a** are allowed to warm from 77 K, a visible color change is observed. Monitoring product conversion by UV−vis spectroscopy over time, $\lambda_{max}$ for **2a** at 516 nm substantially decreases in intensity and shifts to 525 nm, while a very broad,

**Scheme 3. Proposed Route to the Isolated Terminal Hydroxo Species $Ru_2(DPhF)_4OH$**

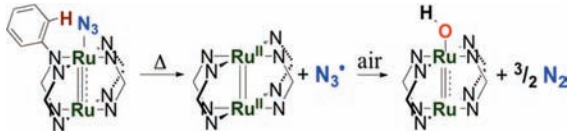


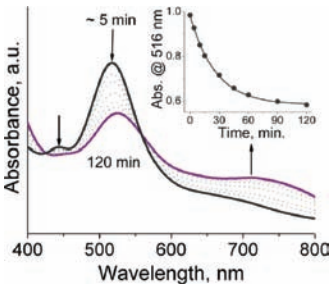


**Figure 5.** Conversion of **2a** to product **3a** followed by UV−vis spectroscopy to completion over 2 h. Inset: absorbance intensity monitored at $\lambda_{max}$(**2a**) = 516 nm.

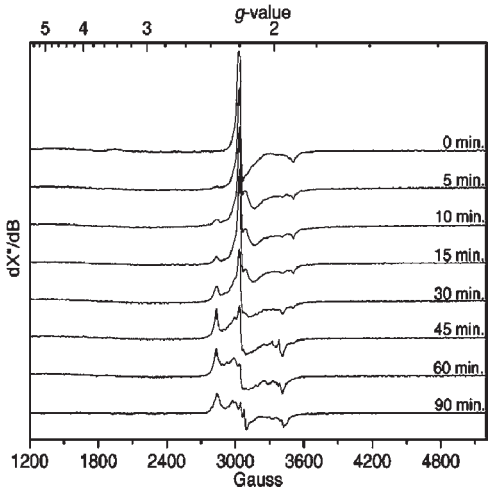


**Figure 6.** Conversion of **2a** to product **3a** by warming from 77 K over 90 min, as followed by EPR spectroscopy.

low-energy signal grows into the spectrum at ~700 nm. As shown in Figure 5, this conversion is clean, showing isosbestic points at ~420 and ~560 nm, indicative of the formation of one product. This reactivity has been observed over a temperature range between 0 and 25 °C. The product shows a mass spectrum identical to that of **3a**, and its IR and UV−vis features are also consistent with its formulation as **3a**.

The conversion of photochemically generated **2a** to **3a** has also been monitored by EPR spectroscopy, revealing that the axial $S = 1/2$ nitride EPR signal (**2a**), with $g_\perp = 2.18$ and $g_\parallel = 1.90$, morphs into a rhombic signal upon warming (Figure 6), with $g_1 = 2.35$, $g_2 = 2.19$, and $g_3 = 1.95$. These $g$ values are practically identical to those we have established[13] for **3a**: $g_1 = 2.34$, $g_2 = 2.14$, and $g_3 = 1.91$ (Figure 7). These EPR data provide further evidence that the thermal conversion product of **2a** is the intramolecularly functionalized product **3a**.

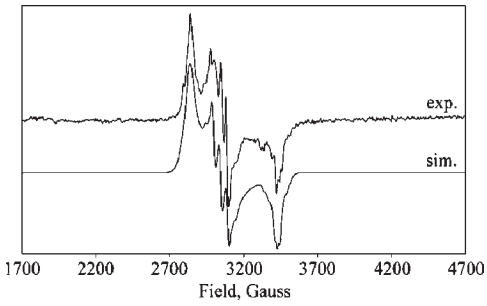


**Figure 7.** X-band EPR spectrum of product **3a** in $CH_2Cl_2$ solution. Experimental data (top signal) measured at 77 K, microwave frequency 9.35791 GHz, power 100.825 $\mu$W, modulation 10.4557 mT. Simulated spectrum (bottom signal) with $g_x = 2.350$, $g_y = 2.192$, and $g_z = 1.947$. Ruthenium hyperfine coupling: $A_x^{Ru} = 23.3 \times 10^{-4}$ cm$^{-1}$, $A_y^{Ru} = 20.0 \times 10^{-4}$ cm$^{-1}$, $A_z^{Ru} = 26.7 \times 10^{-4}$ cm$^{-1}$. Nitrogen superhyperfine coupling: $A_x^N = 16.7 \times 10^{-4}$ cm$^{-1}$, $A_y^N = 46.7 \times 10^{-4}$ cm$^{-1}$, $A_z^N = 13.3 \times 10^{-4}$ cm$^{-1}$.

Thus, we have now provided two pieces of direct evidence for the insertion of a diruthenium nitride into aryl C−H bonds. First, the signature Ru≡N stretch for **2a** at ~850 cm$^{-1}$ was observed to grow in and then disappear in the IR spectrum during thermolytic conversion of **1a** to **3a** in a pressed KBr pellet. Second, we have established that **2a**, isolated in a frozen dichloromethane matrix by photolysis of **1a**, undergoes thermally induced transformation to **3a** at room temperature and below. The photolytic preparation methods described here, in combination with spectroscopic techniques, have allowed stepwise analysis of both of the critical reactions: that of **1a** to form the nitrido intermediate **2a**, and reaction of **2a** via C−H insertion to give **3a**. This result is noteworthy in that, in contrast to other reports of nitride C−H functionalizations at elevated temperatures,[16−20] **2a** performs aryl C−H functionalization at room temperature and below.

**3.5. Kinetics Studies.** The direct observation of the conversion of **2a** to **3a** in solution allows us to now obtain detailed mechanistic information about this C−H functionalization event, information that heretofore has been totally inaccessible for reactions of metal−metal/metal−ligand multiply bonded species with substrate C−H bonds. In order to gain insight into the mechanism of this C−H insertion reaction, temperature-dependent kinetics studies following the formation of **3a** from **2a** by UV−vis spectroscopy were performed over the temperature range from 0 to 25 °C. First-order rate constants for the conversion of **2a** to **3a** were obtained from an exponential fit of the absorbance data, as shown in the inset to Figure 5. The temperature-dependent rate data were modeled with the Eyring−Polanyi equation to determine activation parameters, $\Delta H^\ddagger$ and $\Delta S^\ddagger$, for the nitride C−H insertion event, as illustrated in Figure 8. The resulting $\Delta H$, 89.6 kJ mol$^{-1}$, is somewhat larger than that determined by Nam for intermolecular hydroxylation of anthracene by an Fe(IV)═O oxidant ($\Delta H^\ddagger = 54$ kJ mol$^{-1}$).[47] Due to the relatively small temperature range available, $\Delta S^\ddagger$ is not well defined, but it is small, as expected for an intramolecular reaction.

Additionally, the azide precursor **1a** was synthesized with the perdeuterated ligand (D(D$_5$)PhF = *N*,*N*′-bis(pentadeuteriophenyl)formamidinate) to form **D-1a**. This deuterated compound was accordingly photolyzed to form **D-2a** in frozen $CH_2Cl_2$ solution, and conversion to **D-3a** was monitored by

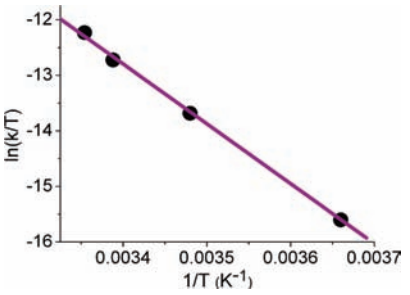


**Figure 8.** Kinetic data fit to the Eyring–Polanyi equation for the reaction temperature range 0–25 °C, where $\ln(k/T) = \{[(-\Delta H^{\ddagger})/R](1/T)\} + \{\ln(k_B/h) + [(\Delta S^{\ddagger})/R]\}$, with $\Delta H^{\ddagger} = 89.6 \pm 2.37$ kJ mol$^{-1}$, $\Delta S^{\ddagger} = 1.0 \pm 8.7$ J mol$^{-1}$, and KIE = $k_H/k_D = 1.1$.

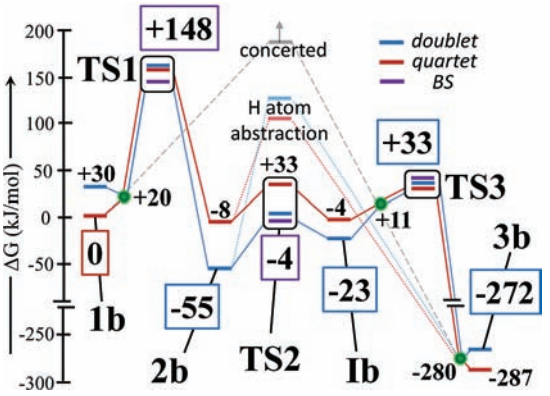


**Figure 9.** Gas-phase B3LYP/B2 energy profile for the intramolecular conversion of **1b** to form **3b** + $N_2$ in the doublet (blue), quartet (red), and BS (purple) states ($\Delta G$, kJ mol$^{-1}$). The Gibbs free energy of a separate $N_2$ molecule was added to **2b**, **TS2**, **Ib**, **TS3**, and **3b**. The green circles indicate minimum energy crossing points between the two spin states. The "concerted" energy (dashed gray) represents a very low estimate of the direct conversion of **1b** to **3b**, bypassing **2b** (*vide infra*). The "H-atom abstraction" energies displayed are lower bounds (*vide infra*).

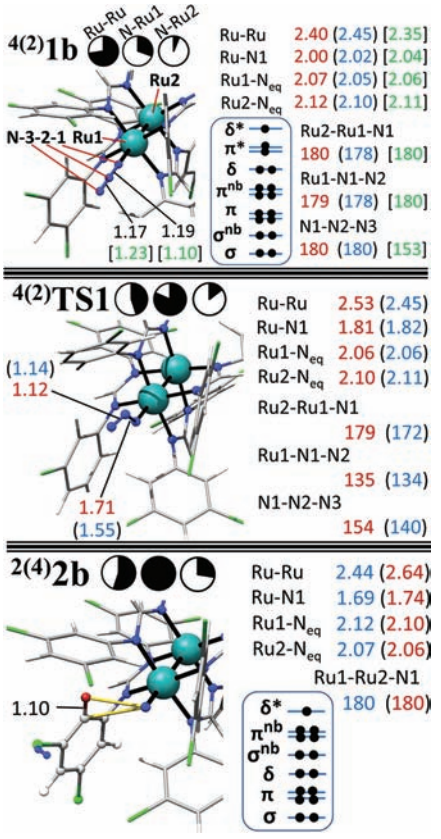


**Figure 10.** Structural information of **1b**, **TS1**, and **2b**. The spin state of the structure pictured corresponds to the $2S + 1$ value to the upper left of the label, with the alternate spin state in parentheses. These are linked with the structural information (distances in Å and angles in °) provided to the right of each picture. Quartet values are red, doublet values are blue, and crystallographic data are green in brackets. Ru–$N_{(eq)}$ indicates the average Ru–N distance to the equatorial N atoms. The pie charts indicate the calculated Mayer bond order (MBO), with a full chart indicating MBO = 2, half-filled MBO = 1, etc. The Ru–Ru MBO is the metal–metal bond, Ru1–N is the nitrido bond, and Ru2–N indicates the degree of three-center bonding in the N1–Ru1–Ru2 moiety. For **1b** and **2b**, the metal–metal bonding molecular orbital diagrams are presented.

UV–vis spectroscopy. From temperature-dependent reaction rates for both the protio and deuterio compounds, a KIE (= $k_H/k_D$) of 1.1 was determined.[56] The KIE allows us to rule out C–H functionalization via H (or D) atom abstraction, since this mechanism should have a KIE significantly greater than 1. The KIE slightly greater than 1 is consistent with results from Que and co-workers on an intramolecular iron–nitrene insertion into aryl C–H bonds that follows an electrophilic aromatic substitution mechanism.[57] More mechanistic implications of the observed KIE will be discussed further in the computational sections below.

**3.6. Density Functional Theory Calculations.** Most prior computational benchmarks for reaction coordinate analysis have been established for mononuclear transition metal complexes, and the metal–metal multiply bonded compounds studied here are, in principle, inherently different, especially with regard to issues of electron correlation between the metals. Thus, the work we present here comparing computational results to experimentally determined energies is an important step toward the development of accurate computational methods for reaction mechanisms involving metal–metal multiply bonded compounds. The calculated reaction coordinate with associated B3LYP/B2 energies is presented in Figure 9 as corrected Gibbs free energies at 298 K. Structural data from BP86/B1 optimizations, B3LYP/B2 Mayer bond orders (MBO), and qualitative molecular orbital (MO) diagrams for **1b**, **2b**, and **3b** are presented in Figures 10 and 11. Figures 12 and 13 focus on the nitride insertion reaction, the former presenting a detailed MO analysis and the latter a Mulliken charge analysis. Selected bond distances and angles for critical species along the reaction coordinate are shown in Table 1. Table 2 breaks down the various energy contributions that sum to $\Delta H$ and $\Delta G$ values relative to **1b** and **2b**. The experimental ground-state assignment of **3b** as a spin doublet comes from low-temperature EPR measurements, and variable-temperature magnetic susceptibility data show a slight increase in $\chi T$ near room temperature,[13] which may indicate a change from $S = 1/2$ to $S = 3/2$. This observation is corroborated by DFT calculations in that calculated enthalpy predicts a doublet ground state, while the Gibbs free energy corrected for entropy at 298 K predicts a quartet ground state. In any case, DFT places these spin states very close together. We have

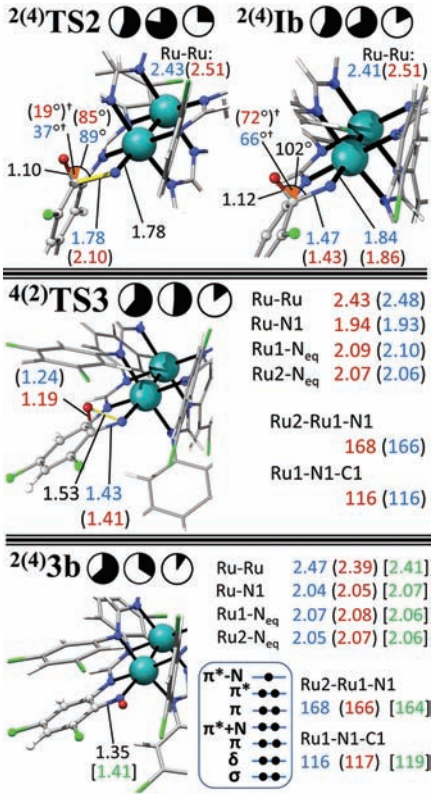


**Figure 11.** Structural information of **TS2**, **Ib**, **TS3**, and **3b**. For **3b**, the metal−metal bonding molecular orbital diagram is presented. See caption of Figure 10 for explanation of structural details. The † symbol denotes the angle between the C−H bond vector and the plane of the aryl ring.

chosen to include only $^2$**3b** in the discussion of electronic structure because it is most relevant to the EPR and crystallographic experimental data.

Before describing the DFT results in detail, it is useful to take stock of the experimentally available information on compounds **1a** and **1b** and their conversion to **3a** and **3b** through the intermediacy of **2a** and **2b**. To aid in benchmarking geometry optimizations, reliable crystal structures are available for **1a**,[12] **1b**,[12] and **3b**,[13] and EXAFS data for **2a** have been reported.[11] Important vibrational data include the azide stretching frequencies of **1a** and **1b**, at 2057 and 2040 cm$^{-1}$, respectively, and the Ru≡N stretch for **2a** of ∼850 cm$^{-1}$.[11] Two valuable pieces of data have been described here involving reaction energetics. First, DSC measurements provide an experimental measure of $\Delta H$ for the conversions of **1a** to **3a** and **1b** to **3b**. The latter value, $\Delta H = -215.2 \pm 12.2$ kJ mol$^{-1}$, is more useful than the former, $\Delta H = -225 \pm 2.5$ kJ mol$^{-1}$, because conversion of **1b** to **3b** is clean and conversion of **1a** to **3a** produces more than one product. Thus, the measured $\Delta H$ for conversion of **1a** to **3a** also includes contributions from other processes and may thus be considered to be a lower limit for the actual $\Delta H$ of the reaction of interest. The second important energetic quantity is the enthalpy of activation, $\Delta H^{\ddagger}$, of the conversion of **2a** to **3a**, measured from variable-temperature kinetic data. The value $\Delta H^{\ddagger} = 89.6 \pm 2.37$ kJ mol$^{-1}$ serves as an experimental benchmark for the transition-state energy between the nitrido compound and its corresponding C−H functionalized product. The conversion of **2a** to **3a** was also found to have a normal but small KIE.

Since thermolysis of **1a** is not clean, and neither is photolysis of **1b**, the important pieces of information have been obtained by studying both compounds, but it was impractical to study both systems computationally. We have therefore chosen to focus on the **1b** to **2b** to **3b** system, for two major reasons. First, more accurate structural data are available for initial geometry optimizations in the **1b** system. Second, the thermal conversion of **1b** to **3b** is not marred by the presence of byproducts, which is an important consideration in that the energetic pathways calculated here represent those that would be available on a thermal, rather than photochemical, pathway. Though we will use the available experimental data from both the **1b** and the **1a** series to benchmark our computational results, the caveats associated with comparing data for two compounds having similar structures but slightly different ligands must be kept in mind.

*3.6.1. Overview of the Reaction Coordinate.* The conversion of **1b** to **2b** was modeled with RSSs that used the N1−N2 bond distance as the constrained variable for both spin surfaces. Each scan produced a maximum energy structure that was used as input for a transition-state search, which yielded transition-state structures $^4$**TS1** and $^2$**TS1**. The lowest energy for **TS1** was obtained from a BS calculation on the quartet geometry (an antiferromagnetically coupled doublet state). The calculated minimum energy pathway then suggests that $^4$**1b** crosses to the doublet surface by way of **mecp1** and proceeds through $^2$**TS1**$_{BS}$ to $^2$**2b** + $N_2$, which is consistent with experimental findings for the ground states of **1b** and **2b**.

The optimized structure of $^4$**1b** (Figure 10) matches the important experimental data reasonably well; however, the structure presents an over-delocalization between the $Ru_2$ core and the axial azide ligand, which is commonly observed with DFT methods. In comparison to the experimental values, the calculated N1−N2 bond distance is elongated by 0.09 Å, the N2−N3 distance is underestimated by 0.06 Å, and the azide ligand is linear, whereas experimentally it is bent with an N1−N2−N3 angle of 152.5°, though this angle is likely an artifact of crystallographic disorder. The structural discrepancies are reflected in the calculated value of $\nu(N_3) = 2211$ cm$^{-1}$, a significant overestimation compared to the experimental value of 2040 cm$^{-1}$. The energy of the system increases by ∼145 kJ mol$^{-1}$ to $^2$**TS1**$_{BS}$ as $^4$**1b** converts to $^2$**2b**. While this occurs, there is significant elongation of the Ru−Ru bond from 2.40 to 2.53 Å and a simultaneous contraction of the Ru1−N1 distance from 2.00 to 1.81 Å as the Ru1≡N1 bond forms. There is also a significant change in the azide moiety that breaks linearity: the Ru−N1−N2 angle changes from 179.2° to 134.6° as the N1−N2 distance elongates from 1.19 to 1.71 Å and N2−N3 contracts from 1.17 to 1.12 Å. The N1−N2−N3 angle is severely bent in the transition state to 138.6°.

Thus, the transition-state structure clearly captures the formation of the Ru1≡N1 nitrido triple bond, the breaking of the N1−N2 bond, and the formation of a new N≡N triple bond in the extruded $N_2$ molecule. Interestingly, this change occurs by an unexpected bending within the azide unit rather than simply losing $N_2$ along the original $Ru_2$−azide vector. This N−N cleavage mechanism is reasonable in light of a similar N−N bond-forming mechanism proposed by Burger for formation of $N_2$ from two terminal nitrido complexes.[19] The system relaxes from **TS1** to the intermediate $^2$**2b**, expelling $N_2$ and gaining 53.1 kJ mol$^{-1}$ in free energy. The Ru−Ru distance snaps back ∼0.1 Å to 2.44 Å as $N_2$ is expelled, and the Ru≡N bond distance becomes 1.69 Å. Both of these distances are in good agreement

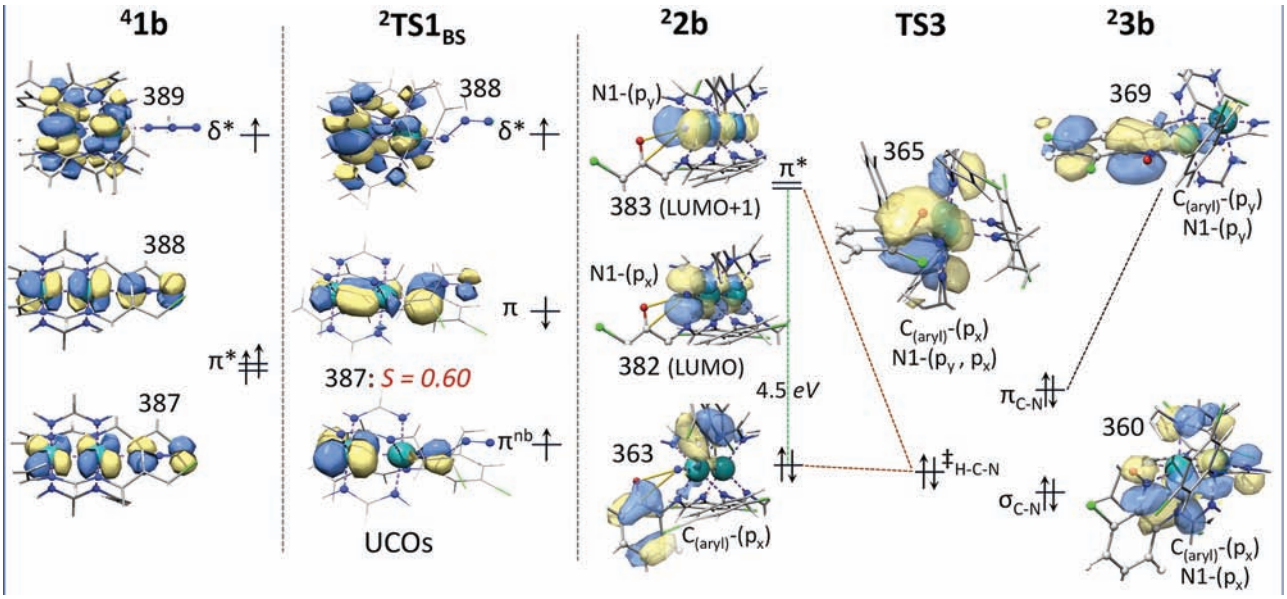


**Figure 12.** Selected MOs for all experimentally observed structures (**1b**, **2b**, and **3b**) and calculated rate-limiting TS structures (**TS1** and **TS3**) that correspond to the reaction coordinate of Figure 9. For $^4$**1b**, the three SOMOs are presented: two degenerate $\pi^*$ (387, 388) and the HOMO $\delta^*$ 389. For $^2$**TS1**$_{BS}$, the corresponding orbital pair (387) is presented, with the overlap integral ($S$ = 0.60) along with the $\delta^*$ HOMO, the singly occupied MO 388. Energy separations for $^4$**1b** and $^2$**TS1**$_{BS}$ are qualitative. The orbitals for $^2$**2b**, **TS3**, and $^2$**3b** are presented in sequence to highlight the nitride C−H bond insertion reaction. For $^2$**2b**, the degenerate $\pi^*$ LUMOs (382, 383) are presented with MO 363, which has large contribution from C1 $p_x$. For **TS3**, orbital 365 is presented, which is a combination of 363, 382, and 383 from $^2$**2b**. For $^2$**3b**, the $\sigma$ and $\pi$ bonds for the newly formed C1−N1 bond are presented. This energy pattern is quantitative, with $\Delta E$ = 4.5 eV between orbital 363 and the $\pi^*$ LUMOs indicated for $^2$**2b**.

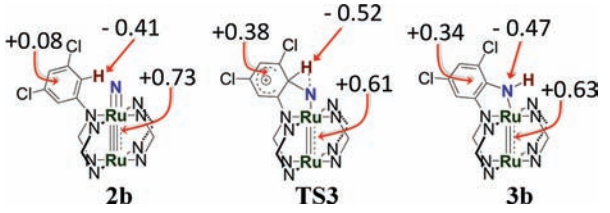


**Figure 13.** Mulliken charges from B3LYP/B2 single-point energy calculations for $^2$**2b**, $^4$**TS3**, and $^2$**3b**. Three charge values are indicated for each figure: (1) ring, (2) N1, and (3) the $Ru_2$ core. The ring charge is the sum of the components, being the six carbons, three hydrogens, and two chlorines of the ring.

with EXAFS data for **2a**. The donor strength of the nitride ligand is evident as the calculated Ru−N$_{(eq)}$ average metal−ligand distances expand slightly from 2.10 Å in $^4$**1b** to 2.12 Å in $^2$**2b**. The energy gap between doublet and quartet nitrido species is ∼50 kJ mol$^{-1}$. In the high-spin excited state of **2b**, the Ru−Ru distance is very long (2.63 Å), and the Ru≡N distance is also elongated from 1.69 to 1.74 Å. A simple explanation for the long distances in the excited-state nitrido species is readily gleaned from the electron configuration of **2b** (Figure 12). In order to have three unpaired electrons, the two LUMO orbitals of $^2$**2b** would have to be occupied, which are antibonding with respect to both the diruthenium core and the Ru1−N1 bond.

A potential mechanism for conversion of **1b** to **3b** was explored whereby concerted N−N cleavage and C−H amination occur in one step. However, the initial approach of the azide moiety to the ring raised the energy higher than that of **TS1**. From this point the energy would only increase as the N−N and C−H bonds were broken. This result, in combination with the unambiguous experimental data, causes us to rule out the possibility of such a concerted reaction mechanism in this system.

The conversion of **2b** to **3b** via an electrophilic aromatic substitution mechanism involves two sequential reaction barriers around an intermediate structure. The first barrier, **TS2**, is associated with N−C bond formation, whereas the second barrier, **TS3**, involves transfer of H$^+$ from C to N. The first step in the reaction was modeled with scans that incrementally decreased the N1−C1 bond distance. Both spin surfaces produced a maximum energy structure that was used as input for a transition-state search, which yielded transition-state structures $^4$**TS2** and $^2$**TS2**. Unconstrained geometry optimization of $^4$**TS2** and $^2$**TS2** led to $^4$**Ib** and $^2$**Ib**, respectively, which are intermediates in the electrophilic aromatic substitution mechanism having four bonds to the ring-bound C to be functionalized. Incrementally contracting the N1−H1 distance from the distance observed in **Ib** to that observed in **3b** led to $^4$**TS3** and $^2$**TS3** on the respective spin surfaces. The calculated pathway indicates that the reaction takes place on the doublet surface from **2b** through **TS2** and **Ib**. The **TS3** energies for quartet and doublet states, as well as BS states, are predicted to be essentially equal, so there appears to be significant flexibility in this state as H1 transfers from C1 to N1 as the system relaxes to $^2$**3b**. The presence of **mecp2** and **mecp3** directly before and after **TS3**, respectively, suggests that the reaction could proceed either through $^4$**TS3** or through a doublet surface. Indeed, we observe that the electronic structure of $^4$**TS3** contains orbitals that are essentially identical to those presented in Figure 12 for $^2$**TS3** to describe the electron-transfer process in the conversion of **2b** to **3b**. The presence of two transition states flanking an intermediate between **2b** and **3b** is consistent with a classical electrophilic aromatic substitution mechanism. Since **Ib** has not been observed experimentally, and $^2$**TS2** is a remarkably low energy barrier connection between **2b** and **Ib**, our discussion will focus on **TS3**, which is calculated to be the rate-limiting barrier for the nitride insertion reaction, as supported by our

**Table 1. Summary of Selected Bond Distances (Å) and Angles (deg) for Critical Species along the Reaction Coordinate for the Conversion of 1b to 3b**

| | $^4$**1b** | | $^4$**TS1** | $^2$**2b** | $^2$**TS3** | $^2$**3b** | |
|---|---|---|---|---|---|---|---|
| | exp | calc | calc | calc | calc | calc | exp |
| Ru1−Ru2 | 2.35 | 2.40 | 2.53 | 2.44 | 2.48 | 2.47 | 2.41 |
| Ru1−$N_{(eq)}$, av | 2.11 | 2.12 | 2.10 | 2.12 | 2.08 | 2.07 | 2.05 |
| Ru2−$N_{(eq)}$, av | 2.06 | 2.07 | 2.06 | 2.07 | 2.07 | 2.05 | 2.05 |
| Ru1−N1 | 2.04 | 2.00 | 1.81 | 1.69 | 2.05 | 2.04 | 2.04 |
| C1−N1 | — | — | — | 2.78 | 1.41 | 1.35 | 1.41 |
| N1−N2 | 1.10 | 1.19 | 1.71 | — | — | — | — |
| N2−N3 | 1.23 | 1.17 | 1.12 | — | — | — | — |
| C1−H1 | — | — | — | 1.10 | 1.24 | — | — |
| N1−H1 | — | — | — | 2.49 | 1.53 | 1.02 | — |
| Ru2−Ru1−N1 | 180.0 | 180.0 | 179 | 180 | 166 | 168 | 164.1 |
| Ru1−N1−C1 | — | — | — | — | 116 | 116 | 119.1 |
| Ru1−N1−N2 | 180.0 | 179 | 135 | — | — | — | — |
| N1−N2−N3 | 152.5 | 180.0 | 154 | — | — | — | — |
| C1−N1−H1 | — | — | — | 22.3 | 47.4 | 113.5 | — |

**Table 2. Calculated Contributions to the Reaction and Activation Free Energies (in kJ mol$^{-1}$) of the Reaction Coordinate Illustrated in Figure 9**[a]

| | $\Delta E_{elec}$ | $\Delta E_{ZPE}$ | $\Delta E_{therm}$ | $\Delta E_{enthalpy}$ | $\Delta E_{entropy}$ | $\Delta H$ | $\Delta G$ |
|---|---|---|---|---|---|---|---|
| | | | | $^4$**1b** = 0 | | | |
| $^4$**TS1**$_{BS}$ | 155.39 | −13.03 | −2.97 | 0.00 | 8.51 | 139.39 | 147.90 |
| $^2$**2b** + $N_2$ | −10.65 | −12.28 | −4.28 | 2.48 | −28.36 | −24.73 | −53.09 |
| $^4$**TS3** + $N_2$ | 84.45 | −20.95 | −2.49 | 2.48 | −34.37 | 63.49 | 29.12 |
| $^2$**TS3** + $N_2$ | 96.33 | −27.54 | 0.32 | 2.48 | −40.31 | 71.59 | 31.28 |
| $^2$**3b** + $N_2$ | −227.38 | −4.86 | 1.37 | 2.48 | −43.57 | −228.40 | −271.97 |
| | | | | $^2$**2b** = 0 | | | |
| $^4$**TS3** | 95.10 | −8.67 | 1.79 | 0.00 | −6.01 | 88.22 | 82.21 |
| $^2$**TS3** | 106.98 | −15.26 | 4.60 | 0.00 | −11.95 | 96.31 | 84.37 |
| $^2$**3b** | −216.73 | 7.41 | 5.64 | 0.00 | −15.21 | −203.67 | −218.88 |

[a] Energies are noted relative to **1b** (top, **1b** = 0) and **2b** (bottom, **2b** = 0).

experimental data. This result is validated by KIE considerations, because **TS2** is expected to give an inverse KIE effect (KIE < 1), which is often observed for electrophilic aromatic substitutions. The C1−H1 bond shows a slight increase in MBO (0.92 to 0.93) from **2b** to **TS2** as H1 breaks from the plane of the aryl ring by 37° and C1 changes from $sp^2$ to $sp^3$ hybridization, consistent with the calculated inverse isotope effects, $KIE_E/KIE_W$ = 0.30/0.30 for the doublet surface and 0.31/0.31 for the quartet surface. In $^2$**TS3** the C1−H1 bond is partially broken and significantly weaker than in **2b**, which is consistent with KIE > 1, calculated from DFT to be $KIE_E/KIE_W$ = 1.02/1.26 for the doublet surface and 0.90/1.08 for the quartet surface. It is rather unusual that C−N bond formation is more facile than proton transfer in this reaction, though this observation is in line with the well-known efficient activity of $Rh_2$ and $Ru_2$ catalysts for nitrenoid insertion into C−H bonds.[2] These results point to a similar electronic origin for the spectacular reactivity of M−M═NR and M−M≡N species.

It is interesting that both spin-state energies for **TS1** and **TS3** occupy an energy window smaller than 20 kJ mol$^{-1}$, within the accepted error for reaction barriers calculated with B3LYP,[40,53] and thus none of these states may be ruled out as viable on purely energetic grounds. Considering the fact that $Ru_2$ complexes are well known in both doublet and quartet ground states, and that even spin-crossover examples exist, it is reasonable that the doublet and quartet energy surfaces are very close together.[58] In addition, the presence of mecps along the reaction coordinate provide flexibility in the interpretation of the calculated reaction pathway. It is apparent that both spin states provide a feasible pathway from **1b** to **2b** and **2b** to **3b**. This mechanistic situation is in contrast to the two-state reactivity principle of Shaik,[52] which is well developed for mononuclear transition metal-oxo complexes where a transition state may be stabilized by increasing the spin multiplicity relative to the ground state of the reactant. Instead, the electronic structure of these binuclear complexes results in a set of closely spaced states of different spin multiplicity, which may be considered to be an important factor for the reactivity of these species.

As the nitrido N atom approaches the aryl C−H bond, the energy of the system increases by ∼80 kJ mol$^{-1}$, going from $^2$**2b** (−53.1 kJ mol$^{-1}$) to $^4$**TS3** (+29.1 kJ mol$^{-1}$) or $^2$**TS3** (+31.3 kJ mol$^{-1}$), in the transformation from $^2$**2b** to $^2$**3b**. Simultaneously, the Ru−Ru distance remains constant at ∼2.44 Å and the Ru1−$N_{(eq)}$ distances contract from 2.12 to 2.09 Å, due to the axial substituent changing from a strongly donating nitrido ligand to a less strongly donating amido species, lengthening from 1.69 to 1.94 Å, coupled with a shift in the axial attack observed in the Ru2−Ru1−N1 angle, changing from ∼180° in $^2$**2b** to ∼167° in **TS3**. As the Ru−N1 bond distance lengthens to 1.94 Å in the transition state, the N1−C1 bond begins to form (1.43 Å) and the C1−H1 bond begins to break, elongating from 1.10 Å in $^2$**2b** to 1.19 Å in $^4$**TS3** or 1.24 Å in $^2$**TS3**.

The system relaxes from **TS3** to yield the amido product $^2$**3b**, completing the transfer of H1 from C1 to N1 and gaining 218.9 kJ mol$^{-1}$ in free energy relative to $^2$**2b**. The Ru−Ru distance elongates by 0.04 Å to 2.47 Å, which is linked with a further contraction of Ru1−$N_{(eq)}$ from 2.09 Å in **TS3** to 2.07 Å in $^2$**3b**. The Ru1−N1 distance continues to lengthen until an equilibrium distance of 2.07 Å is reached in $^2$**3b**, as C1−N1 shortens from 1.43 to 1.35 Å and the N1−H1 distance shrinks from 1.53 to 1.02 Å. The Ru1−N1−C1 angle of 116° from **TS3** is unchanged in $^2$**3b**. The optimized structure of $^2$**3b** matches the experimental crystal structure reasonably well, with several slight deviations: the Ru−Ru distance is overestimated by ∼0.06 Å (at 2.47 Å), and the Ru1−N1 and N1−C1 distances are underestimated by ∼0.03 Å (at 2.04 Å) and ∼0.06 Å (at 1.35 Å), respectively.

The results presented in Figure 9 may be correlated with the experimental energetic results that we report here. We have measured the overall $\Delta H$ for the transformation of **1b** to **3b** by DSC, giving $\Delta H$ = −216 kJ mol$^{-1}$. This result may be compared to the calculated $\Delta H$ for conversion of **1b** to **3b**, which can be computed from the data in Table 2 as the energy of **3b** relative to **1b**, whose energy is set to zero. The $\Delta H$ value corresponds to the sum of the electronic, zero-point, and thermal energies along with the enthalpic correction, yielding a value of $\Delta H$ = −228 kJ mol$^{-1}$, which is in good agreement with $\Delta H$ measured experimentally. Also, the $\Delta H$ and $\Delta S$ of activation for conversion of **2a** to **3a** have been measured: $\Delta H^{\ddagger}$ = 89.6 ± 2.37 kJ mol$^{-1}$ and $\Delta S^{\ddagger}$ = 1 ± 9 J mol$^{-1}$ K$^{-1}$. Although the computations presented here have been performed with the substituted D(3,5-$Cl_2$)DPhF

ligand in which the nitride insertion was first observed, it is reasonable to compare the calculated activation parameters for **TS3** with those determined experimentally using the unsubstituted DPhF ligand. Table 2 includes the thermodynamic data for **TS3** relative to **2b** as an energetic zero point. The calculated $\Delta H^{\ddagger}$ = 88.2 kJ mol$^{-1}$ for $^{4}$**TS3** and 96.3 kJ mol$^{-1}$ for $^{2}$**TS3** are in excellent agreement with the experimental values. The entropic correction, $\Delta S^{\ddagger}$, is calculated to be 6.14 J mol$^{-1}$ K$^{-1}$ on the doublet surface.

It is useful here to compare our calculated reaction pathway (Figure 9) to that proposed by Batista and Kiplinger, involving insertion of a putative uranium nitrido intermediate into an alkyl C−H bond.[18] In general, most of the differences in spin states are larger in the uranium system than those calculated for the diruthenium system, with the exception of the nitrido compound. The nitride is calculated to be high spin for the uranium system, with a triplet−singlet splitting of ∼66 kJ mol$^{-1}$, comparable to the doublet−quartet splitting of 48.3 kJ mol$^{-1}$ in **2b**. The activation barrier toward expulsion of $N_2$ and nitride formation for the uranium complex is more than 50 kJ mol$^{-1}$ higher than that for **1b**. Notably, the proposed uranium nitride is computed to perform alkyl C−H functionalization via a hydrogen abstraction/radical rebound mechanism with a large activation barrier of ∼149 kJ mol$^{-1}$, which is nearly twice as large as the calculated **TS3** for the diruthenium system.

*3.6.2. Electronic Structure and Bonding.* In order to probe the fundamental questions about why the reactivity reported here exists, we turn to a discussion of the electronic structure. Compound $^{4}$**1b** formally has five monoanionic ligands that form an $Ru_2^{5+}$ core with 11 Ru-based electrons. The qualitative MO diagram for $^{4}$**1b** shown in Figure 10 contains 17 electrons in 10 metal−metal bonding type orbitals formed from overlap of $d_{z^2}$, $d_{xz}$, $d_{yz}$, and $d_{xy}$ orbitals. The azide ligand strongly interacts using its N $p_x$, $p_y$, and $p_z$ orbitals to form three-center $\sigma$ and $\pi$ orbitals, formally contributing 6 electrons, leaving the anticipated 11 electrons in the $Ru_2^{5+}$ core. This metal−metal orbital occupation ($\sigma^2\sigma_{nb}{}^2\pi^4\pi_{nb}{}^4\delta^2\pi^{*2}\delta^{*1}$) yields an idealized Ru−Ru bond order of 2.5, significantly greater than the calculated MBO = 1.45. This discrepancy indicates that factors such as poor overlap of $Ru_2$ $\pi$ and $\delta$ orbitals leads to a low computed bond order. The MBO trend for the Ru1−Ru2 and Ru1−N1 bonds, and also the three-center Ru2−N1 MBO, are useful and instructive in the discussion of bonding trends in the conversion from $^{4}$**1b** to $^{2}$**2b**, as well as from $^{2}$**2b** to $^{2}$**3b**.

As expected, the electronic structure of $^{2}$**TS1$_{BS}$** is complicated since the molecular structure is in flux. Rather than describing the electronic configuration of this transition state, we instead will investigate key orbital interactions that are of relevance to the reactivity in this study. The elongated Ru−Ru distance of $^{2}$**TS1$_{BS}$** ($^{4}$**TS1** structure) appears to result directly from a contraction of the Ru1−N1 bond that increases the Ru−N bonding interaction at the expense of Ru−Ru bonding. The orientation of the Ru−N $\sigma$ orbital is skewed in $^{2}$**TS1$_{BS}$** by approximately 45° relative to the Ru−Ru axis due to the severe bend in the departing $N_2$ moiety, which breaks the symmetry of the Ru−Ru bonding orbitals, weakening the overlap. There are two electrons in $^{2}$**TS1$_{BS}$** that are better described as antiferromagnetically coupled than as engaged in bonding. These UCOs are highlighted in Figure 12. Notably, these electrons are both of $\pi$ symmetry with respect to the Ru−Ru bond. Our interpretation of the bonding implications of this diradical state is that the significant elongation of the Ru−Ru distance on transforming from **1b** to $^{2}$**TS1$_{BS}$** causes a rupture in one of the Ru−Ru $\pi$ bonds.

Upon formation of $^{2}$**2b**, the electronic occupation becomes more intuitive, wherein 15 electrons occupy the metal−metal bonding type orbitals with the configuration ($\sigma^2\pi^4\delta^2\sigma_{nb}{}^2\pi_{nb}{}^4\delta^{*1}$). Six of these electrons can be assigned to the $N^{3-}$ ligand, leaving 9 Ru-based electrons corresponding to the $Ru_2^{7+}$ core, producing a net formal Ru−Ru bond order of 3.5, deviating significantly from the computed MBO = 1.10. As we have discussed previously,[11] the $\sigma$ and $\pi$ interactions in this compound engage in delocalized three-center/four-electron Ru−Ru−N bonding, and therefore the three-center/four-electron $\sigma$ and $\pi$ bonds are not as strong as localized two-center orbital interactions, resulting in a lower MBO. The MBO is also likely significantly depressed by the Ru−Ru delta interaction, which we anticipate to be quite weak, with a Ru−Ru distance of 2.44 Å.

Along the reaction coordinate from **1b** to **TS1** to **2b**, the Ru−Ru MBO changes from 1.45 to 0.90 to 1.10, and the long-distance Ru2···N1 MBO changes from 0.12 to 0.29 to 0.55 (see pie charts in Figure 10 for an illustration of this MBO trend). The two-bond MBO is a direct indication of the three-center nature of the bonding interaction in the Ru2−Ru1−N1 moiety. This concept is a direct extension of the analysis of nitride compounds by Bendix, who notes that nitride ligands contribute a large linear component that dominates the ligand field.[59] The three-center MBOs here are consistent with an increasing importance of this Ru−Ru−N interaction, supported by the corresponding Ru1−N1 MBO trend increasing from 0.61 ($^{4}$**1b**) to 1.63 (**TS1**) to 2.09 ($^{2}$**2b**), showing significant multiple bond character of the Ru≡N bond in the nitride compound. Notably, the degenerate LUMOs of **2b** are the Ru−Ru−N $\pi^*$ orbitals that have significant N p character, and these are shown in Figure 12. The electrophilic character of the nitride **2b** is derived from these orbitals.

The key orbital interaction in transition state $^{4,2}$**TS3** results from a combination of the LUMOs of **2b** with filled orbital 363 having significant character deriving from the C−H bond to be functionalized. The doubly occupied orbital 365 ($^{\ddagger}$H−N−C) in **TS3**, shown in Figure 12, is essentially a combination of the three orbitals pictured for **2b**: the C1 $p_x$ orbital 363 and the two LUMOs 382 and 383. We interpret these orbital interactions in **TS3** as a classical electrophilic aromatic substitution transition state for $H^+$ migration. This interpretation is supported by the surface plots of Figure 12, focusing on the central plot of $^{2}$**2b** and moving to the right through **TS3** to $^{2}$**3b** at the right, and is also supported by Mulliken charge analysis (Figure 13). As **TS3** relaxes to $^{2}$**3b**, the C $p_x$ and N $p_x$, $p_y$ orbitals reorganize to form $\sigma$- and $\pi$-bonding interactions between N1 and C1, $^{2}$**3b** orbitals 360 and 369 in Figure 12, consistent with an N−C multiple bond reflected in the calculated MBO = 1.23.

These orbital interactions are consistent with the trend in Mulliken charges[60,61] for the aryl ring of six carbons, three hydrogens, and two chlorines, as well as N1 and the $Ru_2$ core (Figure 13). The Mulliken charges from $^{2}$**2b** to $^{4}$**TS3** to $^{2}$**3b** are then respectively 0.08, 0.38, 0.34 for the aryl ring, −0.41, −0.52, −0.47 for N1, and 0.73, 0.61, 0.63 for the $Ru_2$ core. These Mulliken charges traced from $^{2}$**2b** to $^{4}$**TS3** to $^{2}$**3b** are consistent with the interpretation of this reaction as an electrophilic aromatic substitution and indicate that electron density is transferred from the aryl ring, accumulating on N1 for **TS3**. Upon formation of $^{2}$**3b**, the ring has lost electron density, while N1 and the $Ru_2$ core have both gained electron density.

These results can be rationalized as an observation of the ring electrons becoming delocalized into the diruthenium core through the new anilide moiety in $^2$**3b**.

It is clear from the above computational results and discussion that B3LYP/DFT has successfully recreated the general features of the conversion of **1b** to **3b**, as well as delivered significant insights into the reactivity of **2b**. This is fortunate, as DFT is the only available method able to efficiently treat a multibarrier reaction pathway for a 109-atom complex with two strongly interacting open-shell second-row transition metals. The present study may be considered as a benchmark for future efforts aimed at interpreting in detail the role of metal−metal bonding, along with other aspects of this C−H bond functionalization mechanism.

## 4. SUMMARY AND CONCLUDING REMARKS

We have found in the work reported here that the Ru−Ru bonded paddlewheel motif provides a framework for generating a reactive terminal nitrido species that reacts at room temperature and below with proximal aryl C−H bonds in an intramolecular fashion to yield new aryl C−N bonds. Thermolysis of terminal azido complexes **1a** and **1b** leads to expulsion of $N_2$, observable by differential scanning calorimetry and thermal gravimetric analysis, and subsequent formation of the isolable aryl C−H insertion products **3a** and **3b**, respectively. The corresponding stepwise transformation of **1a** to **3a** by way of the terminal nitrido intermediate complex **2a** was followed by EPR spectroscopy and UV−vis spectroscopy, from which variable-temperature kinetic data could be obtained and modeled. From these kinetic data, we have determined the activation enthalpy and entropy associated with intramolecular insertion of the nitride N atom into the aryl C−H bond. This is the first time that these detailed mechanistic data have been available for a nitride C−H functionalization reaction. DFT calculations have been performed for the entire reaction mechanism for the transformation of **1b** to **2b** to **3b**. The calculated energetics are in good agreement with those determined experimentally, and the orbital analysis of the transition state for nitride C−H insertion is consistent with an interpretation of this reaction as being an electrophilic aromatic substitution reaction, in which the low-lying $\pi^*$ LUMOs of the diruthenium nitride complex lead to its superelectrophilic character. Moreover, the calculated pathways from **1b** to **3b** involve rather closely spaced energetic splitting between quartet and doublet potential energy surfaces. We suggest that the binuclear nature of these diruthenium complexes allows for significant spin state flexibility, which in turn engenders the nitride **2b** with reactivity reminiscent of metal−metal bonded nitrenoid species that have been employed successfully in catalytic C−H amination chemistry.

## ■ ASSOCIATED CONTENT

**Supporting Information.** Additional information, including crystallographic information, for $Ru_2(DPhF)_3NH(C_{13}H_{10}N_2)$ (**3a**), $Ru_2(D(3,5\text{-}Cl_2)PhF)_3NH(C_{13}H_6N_2Cl_4)$ (**3b**), and $Ru_2(DPhF)_4OH$, as well as Figures S1−S11, and relevant *xyz* atomic coordinate data for computed structures. This material is available free of charge via the Internet at http://pubs.acs.org.

## ■ AUTHOR INFORMATION

**Corresponding Author**
berry@chem.wisc.edu

## ■ ACKNOWLEDGMENT

This work is dedicated to the memory of Michelle Millar, whose enthusiasm for inorganic chemistry will be remembered fondly. We thank the U.S. Department of Energy, Chemical Sciences, Geosciences, and Biosciences Division, Office of Basic Energy Sciences, Office of Science (DE-FG02-10ER16204) and the Petroleum Research Fund (50690-ND3) for their support of this work. The computational facilities used were supported by a grant from the National Science Foundation (CHE-0840494). The Hungarian National Research Fund (OTKA PD75360) is acknowledged for work done at the University of Pannonia. Additionally, we are grateful to Dr. Matthew Benning of Bruker AXS and Dr. Ilia Guzei of the University of Wisconsin Chemistry Department for crystallographic assistance.

## ■ REFERENCES

(1) Davies, H. M. L.; Manning, J. R. *Nature* **2008**, *451*, 417–424.
(2) Espino, C. G.; Du Bois, J. Rhodium(II)-Catalyzed Oxidative Amination. In *Modern Rhodium-Catalyzed Organic Reactions*; Evans, P. A., Ed.; Wiley-VCH: Weinheim, 2005.
(3) Doyle, M. P.; Duffy, R.; Ratnikov, M.; Zhou, L. *Chem. Rev.* **2010**, *110*, 704–724.
(4) Bergman, R. G. *Nature* **2007**, *446*, 391–393.
(5) *Handbook of C−H Transformations*, Vol. 2; Dyker, G., Ed.; Wiley-VCH Verlag GmbH and Co. KGaA: Weinheim, 2005.
(6) Doyle, M. P.; Griffin, J. H.; Bagheri, V.; Dorow, R. L. *Organometallics* **1984**, *3*, 53–61.
(7) Wang, Z.; Zhang, Y.; Fu, H.; Jiang, Y.; Zhao, Y. *Org. Lett.* **2008**, *9*, 1863–1866.
(8) Wiese, S.; Badiei, Y. M.; Gephart, R. T.; Mossin, S.; Varonka, M. S.; Melzer, M. M.; Meyer, K.; Cundari, T. R.; Warren, T. H. *Angew. Chem., Int. Ed.* **2010**, *122*, 9034–9039.
(9) Kornecki, K. P.; Berry, J. F. *Chem.—Eur. J.* **2011**, *17*, 5827.
(10) Berry, J. F. *Comments Inorg. Chem.* **2009**, *30*, 1–39.
(11) Pap, J. S.; DeBeer George, S.; Berry, J. F. *Angew. Chem., Int. Ed.* **2008**, *120*, 10102–10105.
(12) Wei-Zhong, C.; De Silva, V.; Lin, C.; Abellard, J.; Marcus, D. M.; Ren, T. *J. Cluster Sci.* **2005**, *16*, 151–165.
(13) Long, A. K. M.; Yu, R. P.; Timmer, G. H.; Berry, J. F. *J. Am. Chem. Soc.* **2010**, *132*, 12228–12230.
(14) Eikey, R. A.; Abu-Omar, M. M. *Coord. Chem. Rev.* **2003**, *243*, 83–124.
(15) (a) Carreira, E. M.; Hong, J.; Du Bois, J.; Tomooka, C. S. *Pure Appl. Chem.* **1998**, *70*, 1097–1103. (b) Man, W.-L.; Lam, W. W. Y.; Yiu, S.-M.; Lau, T.-C.; Peng, S.-M. *J. Am. Chem. Soc.* **2004**, *126*, 15336–15337.
(16) (a) Atienza, C. C. H.; Bowman, A. C.; Lobkovsky, E.; Chirik, P. J. *J. Am. Chem. Soc.* **2010**, *132*, 16343–16345. (b) Schlangen, M.; Neugebauer, J.; Reiher, M.; Schroder, D.; Lopez, J. P.; Haryono, M.; Heinemann, F. W.; Grohmann, A.; Schwarz, H. *J. Am. Chem. Soc.* **2008**, *130*, 4285–4294.
(17) Hennig, H.; Hofbauer, K.; Handke, K.; Stich, R. *Angew. Chem., Int. Ed. Engl.* **1997**, *36*, 408–410.
(18) Thomson, R. K.; Cantat, T.; Scott, B. L.; Morris, D. E.; Batista, E. R.; Kiplinger, J. L. *Nat. Chem.* **2010**, *2*, 723–729.
(19) Schöffel, J.; Šušnjar, N.; Nückel, S.; Sieh, D.; Burger, P. *Eur. J. Inorg. Chem.* **2010**, 4911–4915.
(20) Schöffel, J.; Rogachev, A. Y.; DeBeer, S.; Burger, P. *Angew. Chem., Int. Ed.* **2009**, *48*, 4734–4738.
(21) *SMART*; Bruker-AXS: Madison, WI, 2009.

(22) Sheldrick, G. M. *Acta Crystallogr.* **2008**, *A64*, 112–122.
(23) Dolomanov, O. V.; Bourhis, L. J.; Gildea, R. J.; Howard, J. A. K.; Puschmann, H. *J. Appl. Crystallogr.* **2009**, *42*, 339–341.
(24) Guzei, I. A. Internal Laboratory Computer Programs 'Inserter', 'FCF_Filter', 'Modicifer', 2006−2008.
(25) Cotton, F. A.; Daniels, L. D.; Shang, M.; Yao, Z. *Inorg. Chim. Acta* **1994**, *215*, 103–107.
(26) Neese, F. *ORCA, An Ab Initio, Density Functional and Semi-empirical Program Package*, v. 2.8.0; University of Bonn: Germany, 2009.
(27) Perdew, J. P. *Phys. Rev. B: Condens. Matter* **1986**, *33*, 8822–8824.
(28) Becke, A. D. *Phys. Rev. A: At. Mol. Opt.* **1988**, *38*, 3098–3100.
(29) Weigend, F.; Ahlrichs, R. *Phys. Chem. Chem. Phys.* **2005**, *7*, 3297–2205.
(30) Grimme, S. *J. Comput. Chem.* **2006**, *27*, 1787–1799.
(31) Grimme, S. *J. Comput. Chem.* **2004**, *25*, 1463–1473.
(32) Weigend, F. *Phys. Chem. Chem. Phys.* **2006**, *8*, 1057–1065.
(33) Neese, F. *J. Comput. Chem.* **2003**, *24*, 1740–1747.
(34) H-atom abstraction TS structures could not be attained despite utilization of a full Hessian and a systematic trial of the lowest four modes, as well as separate trials that specified the C1−H1 or N1−H1 bond vectors should be involved in mode. We were convinced the highest energy structures from the RSSs represent a lower bound of the H-atom abstraction pathway.
(35) Baker, J. *J. Comput. Chem.* **1986**, *7*, 385–395.
(36) Vosko, S. H.; Wilk, L.; Nusair, M. *Can. J. Phys.* **1980**, *58*, 1200–1211.
(37) Lee, C. T.; Yang, W. T.; Parr, R. G. *Phys. Rev. B: Condens. Matter* **1988**, *37*, 785–789.
(38) Becke, A. D. *J. Chem. Phys.* **1993**, *98*, 1372–1373.
(39) Neese, F. *J. Phys. Chem. Solids* **2004**, *65*, 781–785.
(40) Neese, F.; Wennmohs, F.; Hansen, A.; Becker, U. *J. Chem. Phys.* **2009**, *356*, 98–109.
(41) Larger than 10% spin contamination for the doublet states in the B3LYP/B2 single-point calculations was observed and could not be removed with change of initial guess or large level shifts. To understand the nature of the spin contamination, BS calculations were employed, with the general result that BS calculations on quartet structures returned higher energies than the standard quartet and doublet states (except in the case of $^2$**TS1**$_{\mathbf{BS}}$) and that BS calculations on the doublet structures converged to the standard doublet solution (with the same $\langle \hat{S}^2 \rangle$). Using the coupling constant $J$ from the BS calculations and an energy difference of $3J$ between doublet and quartet states, it is possible to approximate the energy of a "pure spin doublet" state. However, these corrections were less than 5 kJ mol$^{-1}$, and so uncorrected energies are reported.
(42) Bauschlicher, C. W., Jr.; Ricca, A.; Partridge, H.; Langhoff, S. R. In *Recent Advances in Density Functional Methods, Part II*; Chong, D. P., Ed.; World Scientific Publishing Co.: Singapore, 1997; p 165.
(43) Curtiss, L. A.; Raghavachari, K.; Redfern, P. C.; Pople, J. A. *J. Chem. Phys.* **2000**, *112*, 7374–7383.
(44) Ye, S.; Neese, F. *Inorg. Chem.* **2010**, *49*, 772–774.
(45) Ye, S.; Neese, F. *Curr. Opin. Chem. Biol.* **2009**, *13*, 89–98.
(46) Decker, A.; Chow, M. S.; Kemsley, J. N.; Lehnert, N.; Solomon, E. I. *J. Am. Chem. Soc.* **2006**, *128*, 4719–4733.
(47) de Visser, S. P.; Oh, K.; Han, A. R.; Nam, W. *Inorg. Chem.* **2007**, *46*, 4632–4641.
(48) Ye, S.; Neese, F. *Inorg. Chem.* **2010**, *49*, 772–774.
(49) Pettersen, E. F.; Goddard, T. D.; Huang, C. C.; Couch, G. S.; Greenblatt, D. M.; Meng, E. C.; Ferrin, T. E. *J. Comput. Chem.* **2004**, *25*, 1605–1612.
(50) *Avogadro: An open-source molecular builder and visualization tool*, version 1.01; http://avogadro.openmolecules.net/.
(51) Klamt, A.; Schüürmann, G. *J. Chem. Soc., Perkin Trans.* **1993**, *2*, 799–805.
(52) Kumar, D.; de Visser, S. P.; Sharma, P. K.; Cohen, S.; Shaik, S. *J. Am. Chem. Soc.* **2004**, *126*, 1907–1920.
(53) Melander, L.; Saunders, W. H., Jr. In *Reaction rates of isotopic molecules*; Robert, E., Ed.; Krieger Publishing Co.: Malabar, FL, 1987.
(54) Crystals of **3a** have repeatedly been found to be poorly diffracting. The best crystal structure of **3a** has significant crystallographic problems, including whole-molecule disorder, precluding a detailed discussion of its bond distances and angles, although the structure clearly allows for assignment of the molecular connectivity and verifies its identity as **3a**. $Ru_2(DPhF)_3NH(C_{13}H_{10}N_2)$ (**3a**): monoclinic, $P2/n$; $a$ = 17.77(2) Å, $b$ = 10.323(9) Å, $c$ = 24.16(1) Å; $\beta$ = 101.73(4)°; Ru−Ru = 2.454(2) Å. For additional details, see Supporting Information Figures S3−S6.
(55) $Ru_2(DPhF)_4OH$: monoclinic, $Cc$; $a$ = 14.2462(6) Å, $b$ = 13.5824(5) Å, $c$ = 22.8182(8) Å; $\beta$ = 92.223(2)°; Ru−Ru = 2.3499(2) Å. For additional details, see Supporting Information Figures S7 and S8.
(56) The corresponding Eyring−Polanyi plot determined for **D-1a** is found in Supporting Information Figure S9.
(57) Jensen, M. P.; Mehn, M. P.; Que, L., Jr. *Angew. Chem., Int. Ed.* **2003**, *42*, 4357–4360.
(58) Angaridis, P. In *Multiple Bonds Between Metal Atoms*, 3rd ed.; Cotton, F. A., Murillo, C. A., Walton, R. A., Eds.; Springer: New York, 2005; pp 377−424.
(59) Hedegard, E. D.; Bendix, J.; Sauer, S. P. A. *J. Mol. Struct. THEOCHEM* **2009**, *913*, 1–7.
(60) (a) Ginsberg, A. P. *J. Am. Chem. Soc.* **1980**, *102*, 111–117. (b) Noodleman, L. *J. Chem. Phys.* **1981**, *74*, 5737–5743. (c) Noodleman, L.; Norman, J. G.; Osborne, J. H.; Aizman, A.; Case, D. A. *J. Am. Chem. Soc.* **1985**, *107*, 3418–3426. (d) Noodleman, L. *Inorg. Chem.* **1991**, *30*, 246–256.
(61) Mulliken, R. S. *J. Chem. Phys.* **1955**, *23*, 1833.